Bi-directional Monte-Carlo modelling of solar-induced chlorophyll fluorescence images for 3D vegetation canopies in the DART model

Omar Regaieg, Nicolas Lauret, Yingjie Wang, Jordan Guilleux, Eric Chavanon, Jean-Philippe Gastellu-Etchegorry

International Journal of Applied Earth Observation and Geoinformation 118 (2023) 103254

Contents lists available at ScienceDirect

International Journal of Applied Earth Observation and Geoinformation

journal homepage: www.elsevier.com/locate/jag

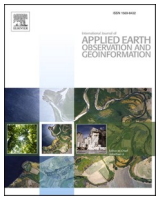

Bi-directional Monte-Carlo modelling of solar-induced chlorophyll fluorescence images for 3D vegetation canopies in the DART model

Omar Regaieg *, Nicolas Lauret, Yingjie Wang, Jordan Guilleux, Eric Chavanon, Jean-Philippe Gastellu-Etchegorry

CESBIO - UPS, CNES, CNRS, IRD, Université de Toulouse, 31401 Toulouse cedex 9, France

ARTICLE INFO

Keywords:
SIF
Remote sensing
Bi-directional path tracing
3D vegetation structure
DART

ABSTRACT

Remote sensing (RS) of solar-induced chlorophyll fluorescence (SIF) has a great potential for monitoring plant photosynthetic activity. Radiative transfer models (RTM) are essential to better interpret and extract information from SIF signals. DART is one of the most comprehensive and accurate 3D RTMs. Its standard mode DART-FT simulates SIF using a discrete ordinates method but is not adapted to large landscapes due to computational constraints. DART-Lux, the new mode based on a bi-directional path tracing algorithm, greatly improves DART computational efficiency for simulating images. This paper presents the theory of a novel SIF modelling algorithm in DART-Lux. We verified its accuracy with DART-FT and the SCOPE model for three types of canopies: turbid medium, maize field and forest. DART-Lux closely matches DART-FT (relative difference $< 2\%$) with much better computational efficiency depending on the scene complexity, number of spectral bands and needed accuracy. For example, simulation time is reduced by a factor of $\approx$48, and memory usage by $\approx$50 for a maize field at 1 cm resolution. It allowed to simulate SIF images of large scenes as the $3 \times 3\,km^2$ Ripperdan agricultural site that DART-FT could not simulate. The new SIF modelling algorithm opens new horizons for RS studies of large and complex landscapes. It is available as part of released DART versions (v1152 onwards) (https://dart.omp.eu/).

1. Introduction

Solar-induced fluorescence (SIF) of vegetation is a spontaneous radiation re-emission from 640 to 850 nm due to absorbed sunlight from 400 to 750 nm. In competition with the photochemical and heat dissipation processes, it allows an electron from a chlorophyll molecule excited by absorbing a quantum of light, to dispose of its excess energy. It provides valuable information on real-time plants photosynthetic activity (Mohammed et al., 2019) which enables early stress detection (Song et al., 2018) and gross primary production (GPP) estimation (Zhang et al., 2020).

The fluorescence quantum efficiency (FQE) of chlorophyll in vivo does not exceed 10%, with typical values under steady-state illumination of 0.5–3% (Porcar-Castell et al., 2014). Hence, the SIF remote sensing (RS) signal is a small fraction of sunlight scattered by a vegetation canopy. The resulting difficulty in interpreting SIF RS signal in terms of vegetation functioning traits is largely amplified by the dependence of the SIF signal on the vegetation 3D structure, combined with illumination and observation conditions (Hornero et al., 2021; Regaieg et al., 2021). This stresses the importance of physical models to link the within canopy SIF emission with RS signals. An ideal radiative model of SIF includes two major sub-models: (1) Leaf SIF emission model considering the incident spectral irradiance, leaf structure and biochemistry, and the probability of a photon absorbed by photosystems I (PSI) and II (PSII) to be re-emitted as SIF (*i.e.*, FQE) derived from leaf physiological modelling. (2) Radiative transfer (RT) model of the radiation propagation in the canopy to simulate the SIF radiance at the bottom and/or top of the atmosphere (*i.e.*, RS signal).

Here, we consider top of canopy SIF modelling including vegetation 3D architecture. Canopy SIF models are generally canopy reflectance models with an imbedded leaf-level fluorescence model. For example, FLSAIL (Rosema et al., 1991), FluorSAIL (Miller, 2005) and SCOPE (van der Tol et al., 2009) models combine leaf SIF modelling with the SAIL canopy reflectance model (Verhoef, 1984). SAIL is one-dimensional (1D), as it represents vegetation as superimposed homogeneous layers filled by a turbid medium: infinite number of infinitely small plane elements characterized by a statistical leaf angular distribution (LAD), a leaf area index (LAI), and optical properties. It simulates the radiative

* Corresponding author.

https://doi.org/10.1016/j.jag.2023.103254
Received 20 October 2022; Received in revised form 26 January 2023; Accepted 28 February 2023
Available online 13 March 2023

transfer with: a source term for direct solar radiation, one stream for upward and one stream for downward fluxes, and the scattered radiance is integrated along the observation direction. SCOPE is a reference model for 1D SIF modelling (Damm et al., 2015; Verrelst et al., 2019). The 1D models' major limitation is neglecting the vegetation horizontal heterogeneity. Accounting for vertical heterogeneity as in mSCOPE (Yang et al., 2017) only partly improves the situation. Indeed, the canopy horizontal heterogeneity has usually a much greater influence on RS signals than vertical heterogeneity (Regaieg et al., 2021). Some approaches aiming to simulate SIF at the global scale account for the influence of the canopy horizontal heterogeneity using clumping indices (Braghiere et al., 2021). However, they cannot fully capture the actual canopies 3D architecture including local topography, and the presence of woody elements, that impact remotely sensed SIF signals (Malenovský et al., 2021; Regaieg et al., 2021).

3D SIF RTMs adapted to realistic vegetation canopies descriptions represented as facets or 3D turbid medium are of great interest because of the 1D models limitation. For example, FLiES-SIF (Sakai et al., 2020) simulates SIF tree canopies having geometrically simple crowns (*e.g.*, cone, cylinder, spheroid) whereas FluorFLIGHT (Hernández-Clemente et al., 2017), FluorWPS (Zhao et al., 2016), DART (Malenovský et al., 2021) and FluCVRT (Kallel, 2020) simulate SIF for any canopy type. FluCVRT includes 3D leaf-level SIF modelling. These models use Monte Carlo ray tracing techniques, apart from DART that uses an adapted forward discrete ordinates method, called DART-FT (Flux Tracking). DART-FT simulates the canopy SIF radiance and reflectance images, the canopy 3D SIF radiative budget (RB) per photosystem, and therefore the canopy fluorescence escape factor (Guanter et al., 2014). DART-FT SIF modelling has been validated with model comparison (Malenovský et al., 2021), and successfully used in various SIF studies such as sensitivity analysis of the SIF signal in architecturally complex forest canopies (Liu et al., 2019a; Malenovský et al., 2021), scaling canopy-level SIF down to photosystems level (Liu et al., 2019b), and studying the far-red SIF escape probability from forest canopies (W. Liu et al., 2020).

Compared to 1D models, 3D models use more parameters, are more computationally demanding and therefore are not well adapted to regional or global scales. Indeed, forward models like DART-FT spend much time and memory tracking fluxes that contribute little to the simulated images. Based on the Bidirectional Path Tracing (BDPT) algorithm (Veach, 1998), based on Monte Carlo modelling, the new DART mode called DART-Lux (Wang et al., 2022) highly reduces computer time and memory requirements to simulate images of large and complex landscapes. Therefore, we designed a novel SIF modelling method adapted to the BDPT algorithm for accurate and computationally efficient simulations of SIF RS images of 3D vegetation canopies. To our knowledge, no similar SIF modelling method has ever been developed for BDPT algorithms.

2. DART-Lux

DART is an accurate and comprehensive 3D RT model developed at CESBIO since 1992 and patented in 2003. It simulates RS images of VIS / NIR / TIR spectro-radiometers, LiDAR observations, and 3D RB of natural and urban landscapes (Wang et al., 2020). Its standard mode, DART-FT, represents landscapes by 3D arrays of voxels filled with facets (*e.g.*, vegetation, buildings), turbid medium and fluids. It iteratively tracks radiation in a user-defined number of discrete directions. DART-Lux, DART's latest mode (Wang et al., 2022), uses the BDPT algorithm with Monte Carlo integration techniques. It can largely decrease time and memory requirements for DART images simulation of large and complex landscapes. It uses the geometry instance, "depth-first" approaches (Cormen et al., 2009) and the BDPT algorithm (Pharr et al., 2016) that preferentially tracks fluxes that contribute most to observations by constructing paths that start both from the sensor and light sources. It is adapted to any configuration with any light sources and landscape elements with any Bidirectional Scattering Distribution Function (BSDF). The radiance measurement $L^{(j)}$ of pixel j of the simulated image is:

$$L^{(j)} = \int_D C^{(j)}(\bar{p})dA(\bar{p})$$

where $\bar{p}$ is a light transport path,

$\mathscr{D}$ is the set of all light transport paths. $\mathscr{D} = \bigcup_{k=1}^{\infty}\mathscr{D}_k$, with $\mathscr{D}_k$ the set of all paths $\bar{p}_k = (p_0,\cdots,p_k)$ of length k (*i.e.*, k segments, $k+1$ vertices p_i; $i\in[0,k]$, p_0 on the sensor, p_k on the light source), $dA(\bar{p})$ is the area product for path $\bar{p}$; *e.g.*, $dA(\bar{p}_k) = dA(p_0)\cdots dA(p_k)$ with area $dA(p_i)$ at vertex i and $C^{(j)}(\bar{p})$ is the contribution function of path $\bar{p}$ to the measurement $L^{(j)}$ of pixel j.

$L^{(j)}$ is computed as:

$$L^{(j)} = \iint_{A_0\Omega_0} W_e^{(j)}(p_0,\Omega)\cdot L(p_1\rightarrow p_0)\cdot|\cos\theta_i^{p_0}|\cdot d\Omega dA(p_0) \quad (1)$$

where A_0 is lens area,

Ω_0 is the solid angle that encloses all incident directions from the optical system to the sensor plane,

$W_e^{(j)}(p_0,\Omega)$ is the importance function (Nicodemus, 1978),

$\theta_i^{p_0}$ is the angle between the incident direction and the sensor principal optical axis and $L(p_1\rightarrow p_0) = \sum_{k=1}^{\infty}L(\bar{p}_k)$ is the radiance at sensor's vertex p_0 from a surface's vertex p_1 with $L(\bar{p}_k)$ the radiance incident on p_0 due to all paths $\bar{p}_k$ of length k; *e.g.*, $\bar{p}_k = (p_k,\cdots,p_1,p_0)$.

The radiance incident at vertex p_i of a path $\bar{p}_k$ is the radiance from the vertex p_{i+1} that illuminates the vertex p_i. A path results of the connection of a vertex of the sensor sub-path created with t vertices from the sensor and a vertex of the source sub-path created with s vertices from the light source. Fig. 1 shows a case with four vertices (p_0, p_1, p_2, p_3), with p_0 on the sensor and p_3 on the source. In DART-Lux, the maximum scattering order (*i.e.*, number of ray bounces on the scene surfaces) is a user-defined parameter. It defines the maximum length of the light transport paths. In this figure, this maximum length is three ($k = 3$: 4 vertices and 3 segments) and the scattering order is 2.

In DART-Lux, the BDPT algorithm estimates $L^{(j)}$ at sensor p_0 from the contributions of sampled paths constructed by incremental path tracing from both the light source and the sensor. For example, if a path $\bar{p}_k$ starts from the sensor, a point p_0 is randomly sampled on the senor and a ray is traced from p_0 and in the direction defined by the sensor properties, until intersecting a surface at a point p_1. Then, the path is iteratively constructed using the two steps:

(1) At each vertex p_i, starting from $i = 1$, sample a new direction according to the BSDF, knowing the incident direction. Stop if $i = k$.
(2) Find the next vertex p_{i+1} by tracing a ray from p_i along the sampled direction.

A Monte Carlo integration technique estimates the pixel radiance measurement with an importance sampling technique (Kalos & Whitlock, 1986). Paths that most impact the radiance reaching the sensor have a higher probability to be sampled. Multiple Importance Sampling (MIS) (Veach & Guibas, 1995) is used to combine the different ways to sample the same path (*e.g.*, Fig. 1b shows the five ways to sample the path in Fig. 1a) using weighting functions that give the weight $w_i(x)$ per sample x drawn from the sampling way i. The Russian Roulette (Veach & Guibas, 1995) is used to randomly stop the calculation at a certain path length to save computer time. A probability q is set to stop a ray and not to evaluate the integrand for the particular sample, and a probability $(1\text{-}q)$ to evaluate the integrand and to weight it by $\frac{1}{1-q}$, to account for all

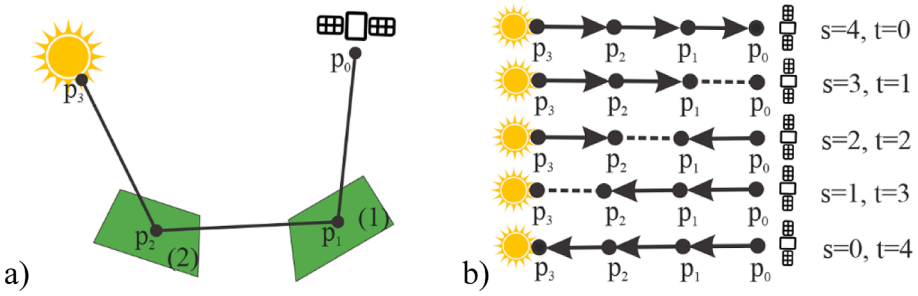

Fig. 1. (a) Path $\bar{p}_3$ with four vertices p_i (i ∈ {0..k} with k = 3). (b) The five ways to construct $\bar{p}_3$, with s and t vertices (s + t = k + 1 = 4) for the sources and sensor sub-paths, respectively.

the samples that are not evaluated. The theory of DART-Lux was presented in more details by Wang et al. (2022).

The DART-Lux image (5 m resolution, 100 bands in [400–850 nm]) of the 3 × 3 km^2 Ripperdan agricultural site with vines and more than 600.000 trees (Fig. 12b) shows its potential. It needed 16.9 GB of memory and 13 min 4 s of simulation time with an Intel Xeon W-2295 CPU @ 3.00 GHz (18 cores, 36 threads). DART-FT was not run because it needed about 50 TB of memory and 1600 h of simulation time.

3. DART-Lux canopy SIF modelling

Despite its interest in accurate and fast radiance simulations of large landscapes, to our knowledge, the BDPT algorithm has never been applied to canopy SIF modelling. Its adaptation to SIF modelling in DART-Lux is presented here. It relies on the surface form of the Light Transport Equation (LTE) to compute as an integral over all scene surfaces A the radiance reaching a vertex p from a vertex p' (Fig. 2):

$$L(p'\to p) = L_e(p'\to p) + \int_A f(p''\to p'\to p)\cdot L(p''\to p')\cdot G(p''\leftrightarrow p')\cdot dA(p'') \quad (2)$$

where $L_e(p'\to p)$ is the radiance emitted from p' to p, if p' belongs to a light source, $L_e(p'\to p) = 0$ otherwise,

$G(p''\leftrightarrow p') = V(p''\leftrightarrow p')\cdot\frac{|cos\theta_0''|\cdot|cos\theta_i'|}{||p'-p''||^2}$ with index o for outgoing and index i for incident,

$f(p''\to p'\to p)$ is the BSDF of surface Σ,

$L(p''\to p')$ is the radiance reaching p' from p'',

V is the binary visibility function: $V(p''\leftrightarrow p') = 1$ if p' and p'' are mutually visible, and 0 otherwise,

$cos\theta_0'' = \overrightarrow{n''}\cdot\frac{\overrightarrow{p''p'}}{||p'-p''||}$ and $cos\theta_i' = \frac{\overrightarrow{p'p''}}{||p'-p''||}\cdot\overrightarrow{n'}$

$\overrightarrow{n'}$ and $\overrightarrow{n''}$ are the normal vectors to the surface Σ at p' and to the surface A at p'', respectively.

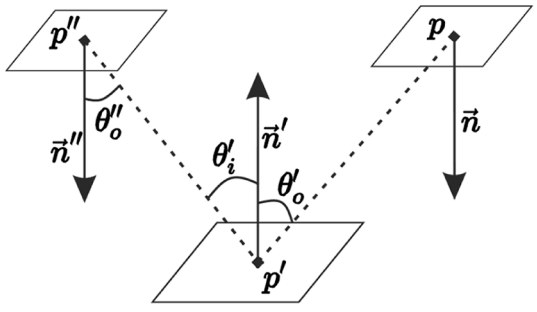

Fig. 2. LTE geometry: the vertex p' scatters the ray coming from the vertex p'' towards the vertex p.

Expanding Eq (2) by iteratively replacing $L(p''\to p')$ by its right-hand term gives $L(\bar{p}_k)$ for $k \geq 2$:

$$L(\bar{p}_k) = \iint_{AA}\int_A L_e(p_k\to p_{k-1})\cdot \left(\prod_{i=1}^{k-1} f(p_{i+1}\to p_i\to p_{i-1})\cdot G(p_{i+1}\leftrightarrow p_i)\right)\cdot dA(p_2)\ldots dA(p_k) \quad (3)$$

We denote $P(\bar{p}_k)$ (Eq (5)) the integrand in Eq (3), and $T(\bar{p}_k)$, the "light path throughput", the term between brackets in $P(\bar{p}_k)$:

$$T(\bar{p}_k) = \prod_{i=1}^{k-1} f(p_{i+1}\to p_i\to p_{i-1})\cdot G(p_{i+1}\leftrightarrow p_i) \quad (4)$$

$$P(\bar{p}_k) = L_e(p_k\to p_{k-1})\cdot T(\bar{p}_k) \quad (5)$$

If p_i belongs to a bi-Lambertian surface, with normal vector $\overrightarrow{n}_i$, reflectance ρ_i and transmittance τ_i:

$$f(p_{i+1}\to p_i\to p_{i-1}) = \begin{cases} \frac{\rho_i}{\pi}, if\ (\overrightarrow{p_ip_{i+1}}\cdot\overrightarrow{n_i})\cdot(\overrightarrow{p_ip_{i-1}}\cdot\overrightarrow{n_i}) \geq 0 \\ \frac{\tau_i}{\pi},\ \text{otherwise} \end{cases} \quad (6)$$

As for DART-FT (Malenovský et al., 2021), the Fluspect model (Vilfan et al., 2018) is used to simulate leaf-level SIF. It uses the leaf biochemical properties and FQEs input parameters to compute four leaf Excitation-Emission Fluorescence Matrices (EEFMs) $M_{x,y,ij}$ for the N user defined spectral bands ($i \in \{1..N\}$ for excitation and $j \in \{1..N\}$ for emission), for the photosystem x (PSI or PSII) and direction y (forward or backward). The reflectance ρ and EEFM backward matrices ($M_{x,backward,ij}$) play equivalent roles for scattering and SIF emission respectively, and so do the surface transmittance τ and EEFM forward matrices ($M_{x,forward,ij}$). In the Fluspect model, the leaves are bi-Lambertian and SIF emitted radiance is isotropic. Therefore, the direction sampling method for SIF is the same as for scattering by bi-Lambertian surfaces with the PDF $p(\Omega) = \frac{\cos\theta}{\pi}$ where θ is the angle between the surface normal and the sampled direction Ω, for any incident direction.

To estimate the pixel radiance measurement, the contribution of each sampled path is evaluated by multiplying the integrand $P(\bar{p}_k)$ of Eq (3) by the importance function and the cosine term in Eq (1).

For N simulated spectral bands, the light source spectral radiance L_e, the bi-Lambertian surface spectral reflectance and transmittance, and also the sub- and full-path throughputs are vectors of N elements. A path throughput is computed by successive element wise vector multiplications of the multi-spectral reflectance or transmittance value at each vertex by a geometric term G, divided by π(Eq (4), (6)). This product is associative and can be computed starting from the light source or starting from the sensor. A full path being the connection of a light sub-path and a sensor sub-path, its throughput is the element wise product of the light and sensor sub-path throughputs. Its multiplication by the light source radiance $L_e(p_k\to p_{k-1})$ gives the integrand $P(\bar{p}_k)$.

For the simplicity of the equations below, we avoid writing the scalar

multiplicative terms G and $\frac{1}{\pi}$. The $\propto$ symbol is used to denote the equality up to a scalar multiplier. If the SIF emission is considered, three components of the radiance need to be computed: 1) the total radiance including the scattered radiation plus SIF radiation, 2) the PSI SIF radiance component, 3) the PSII SIF radiance component. For N simulated spectral bands, a fluorescent surface S_l is characterized by four $N \times N$ EEFMs, in addition to its non-fluorescent BSDF. For photosystem x and for direction y, the EEFM is:

$$M^l_{xy} \propto \begin{pmatrix} f^l_{xy1,1} & \cdots & f^l_{xy1,N} \\ \vdots & \ddots & \vdots \\ f^l_{xyN,1} & \cdots & f^l_{xyN,N} \end{pmatrix}$$

where $f^l_{xyi,j}$ is the EEFM element for an excitation spectral band (central wavelength: λ_i, bandwidth: $\Delta\lambda_i$) and an emission band $(\lambda_j, \Delta\lambda_j)$,

For a path with two segments, the integrand of SIF radiance component of photosystem x and direction y is the matrix product of the light source spectral radiance L_e and the EEFM M_{xy}:

$$P_x(\bar{p}_2) \propto L_e \times M^l_{xy} = (e_1, e_2, \cdots, e_N) \times \begin{pmatrix} f^l_{xy1,1} & \cdots & f^l_{xy1,N} \\ \vdots & \ddots & \vdots \\ f^l_{xyN,1} & \cdots & f^l_{xyN,N} \end{pmatrix} = \left(\sum_{i=1}^{N} e_i . f^l_{xyi,1}, \cdots, \sum_{i=1}^{N} e_i . f^l_{xyi,N} \right)$$

Therefore, for a path $\bar{p}_k$ with $k+1$ vertices p_l, $l \in \{0..k\}$, the integrand for the total radiance (*i.e.*, sum of scattered radiance, PSI and PSII SIF radiance) is:

$$P_{total}(\bar{p}_k) \propto L_e \times T_{tot}(\bar{p}_k) \tag{7}$$

where $T_{tot}(\bar{p}_k) \propto T^1_{\text{tot}} \times \cdots \times T^{k-1}_{\text{tot}}$ is the total throughput,

$$T^l_{\text{tot}} \propto R_l + M^l_{PSIy} + M^l_{PSIy} = \begin{pmatrix} r^l_1 + f^l_{\text{PSIy1,1}} + f^l_{\text{PSIIy1,1}} & \cdots & f^l_{\text{PSIy1,N}} + f^l_{\text{PSIIy1,N}} \\ \vdots & \vdots & \vdots \\ f^l_{\text{PSIyN,1}} + f^l_{\text{PSIIyN,1}} & \cdots & r^l_{\text{N}} + f^l_{\text{PSIyN,N}} + f^l_{\text{PSIIyN,N}} \end{pmatrix}$$

r^l_i is the reflectance or transmittance of the surface S_l at the band $(\lambda_i, \Delta\lambda_i)$, $R_l \propto \begin{pmatrix} r^l_1 & \cdots & 0 \\ \vdots & \ddots & \vdots \\ 0 & \cdots & r^l_N \end{pmatrix}$, and $f^l_{PSIyi,j}$ and $f^l_{PSIIyi,j}$ the EEFM elements for an excitation band $(\lambda_i, \Delta\lambda_i)$ and an emission band $(\lambda_j, \Delta\lambda_j)$ for PSI and PSII respectively, for direction y.

As the matrix product is associative, the product in Eq (7) can be cut into a light sub-path sub-product (*i.e.*, N-element vector resulting from successive vector–matrix products), and a sensor sub-path sub-product (*i.e.*, $N \times N$ matrix resulting from successive matrix–matrix products). However, Eq (7) provides only the total radiance (N-element vector). To have the PSI and PSII radiance separately as well, two additional N-element vectors need to be computed. For the path $\bar{p}_k$, in addition to $P_{total}(\bar{p}_k)$, the $P_{PSI}(\bar{p}_k)$ and $P_{PSII}(\bar{p}_k)$ need to be computed. For a light path $\bar{p}_3$ with 3 segments (two fluorescent surfaces) (Fig. 1), $P_{PSI}(\bar{p}_3)$ and $P_{PSII}(\bar{p}_3)$ are:

$$P_{PSI}(\bar{p}_3) \propto L_e \times \left[T^1_{tot} \times M^2_{PSIy} + M^1_{PSIy} \times R_2 \right] \tag{8}$$

$$P_{PSII}(\bar{p}_3) \propto L_e \times \left[T^1_{tot} \times M^2_{PSIIy} + M^1_{PSIIy} \times R_2 \right] \tag{9}$$

The bracketed terms in Eq (8) and (9) represent the interactions between the two surfaces that generate the two SIF radiance components. Eq (8) and (9) cannot be written as an associative product of terms each of which depends on the properties of a single vertex. Thus, they cannot be computed starting both from the light source and from the sensor. Therefore, the block matrix M^l_B is introduced:

$$M^l_B \propto \begin{pmatrix} T^l_{\text{tot}} & M^l_{PSIy} & M^l_{PSIIy} \\ 0 & R_l & 0 \\ 0 & 0 & R_l \end{pmatrix}$$

The light source radiance vector is also written as a block matrix: $L_{e,B} = (L_{e,total}; L_{e,PSI}; L_{e,PSII})$, where $L_{e,total}$, $L_{e,PSI}$ and $L_{e,PSII}$ are N-element vectors. Since light sources do not emit SIF, $L_{e,PSI}$ and $L_{e,PSII}$ are null vectors. If M^{k-1}_B is the block matrix of the first surface hit by the light source, the incident radiance vector $L_{B,k\text{-}2} \propto L_{e,B} \times M^{k-1}_B$ at vertex k-2 is:

$$L_{B,k\text{-}2} \propto (L_{e,total}; 0; 0) \times \begin{pmatrix} R_{k-1} + M^{k-1}_{PSIy} + M^{k-1}_{PSIIy} & M^{k-1}_{PSIy} & M^{k-1}_{PSIIy} \\ 0 & R_{k-1} & 0 \\ 0 & 0 & R_{k-1} \end{pmatrix}$$

$$= \left(L_{e,total} \times \left(R_{k\text{-}1} + M^{k-1}_{PSIy} + M^{k-1}_{PSIIy} \right); L_{e,total} \times M^{k-1}_{PSIy}; L_{e,total} \times M^{k-1}_{PSIIy} \right)$$

$$= (L_{total,k\text{-}2}; L_{PSI,k\text{-}2}; L_{PSII,k\text{-}2})$$

Similarly, at vertex k-3, the incident radiance vector $L_{B,k\text{-}3} \propto L_{B,k\text{-}2} \times M^{k-2}_B$ is:

$$L_{B,k\text{-}3} \propto (L_{total,k\text{-}2}; L_{PSI,k\text{-}2}; L_{PSII,k\text{-}2}) \times \begin{pmatrix} R_{k\text{-}2} + M^{k-2}_{PSIy} + M^{k-2}_{PSIIy} & M^{k-2}_{PSIy} & M^{k-2}_{PSIIy} \\ 0 & R_{k\text{-}2} & 0 \\ 0 & 0 & R_{k\text{-}2} \end{pmatrix}$$

$$= (L_{total,k\text{-}2} \times (R_{k\text{-}2} + M^{k-2}_{PSIy} + M^{k-2}_{PSIIy}); L_{total,k\text{-}2} \times M^{k-2}_{PSIy} + L_{PSI,k\text{-}2} \times R_{k\text{-}2}; L_{total,k\text{-}2} \times M^{k-2}_{PSIIy} + L_{PSII,k\text{-}2} \times R_{k\text{-}2})$$

$$= (L_{total,k\text{-}3}; L_{PSI,k\text{-}3}; L_{PSII,k\text{-}3})$$

And so on, for each vertex p_l of the light sub path until reaching the sensor, the exiting radiance block matrix is:

$$L_{B,l} \times M_{B,l} \propto (L_{total,l}; L_{PSI,l}; L_{PSII,l}) \times \begin{pmatrix} R_l + M^l_{PSIy} + M^l_{PSIIy} & M^l_{PSIy} & M^l_{PSIIy} \\ 0 & R_l & 0 \\ 0 & 0 & R_l \end{pmatrix}$$

$$= \left(L_{total,l} \times \left(R_l + M^l_{PSIy} + M^l_{PSIIy} \right); L_{total,l} \times M^l_{PSIy} + L_{PSI,l} \times R_l; L_{total,l} \times M^l_{PSII} + L_{PSII} \times R_l \right)$$

All components of the total, PSI and PSII spectral radiance terms of p_l are considered:

- Total radiance $L_{total,l} \times \left(R_l + M^l_{PSIy} + M^l_{PSIIy} \right)$ of surface p_l hit by a ray of incident radiance.$L_{total,l}$
- PSI radiance: sum of the emitted PSI radiance $L_{total,l} \times M^l_{PSIy}$ at p_l due to $L_{total,l}$, and PSI radiance $L_{PSI,l} \times R_l$ coming from the previous vertex and scattered at p_l.
- PSII radiance: sum of the emitted PSII radiance $L_{total,l} \times M^l_{PSII}$ at p_l due to $L_{total,l}$, and PSII radiance $L_{PSII,l} \times R_l$ coming from the previous vertex and scattered at p_l.

These equations can be used starting from the light source and starting from the sensor because they include associative products of matrices and each matrix depends on the properties of a single vertex.

For a light path with $L+2$ vertices (*i.e.*, L hit surfaces of matrices M_B^l with $l \in \{1..L\}$), the integrand $P_B(\overline{p}_{L+2})$ including the total, PSI and PSII signals from this path is:

$$P_B(\overline{p}_{L+2}) \propto L_{e,B} \times M_{B,1} \times M_{B,2} \times \cdots \times M_{B,L}$$

If the light path $\overline{p}_{L+2}$ has S vertices in the light sub-path and T vertices in the sensor sub-path, excluding the light source and sensor vertices ($L+2 = S+T$), the throughput of the light sub-path is $M_B^{\text{light}} \propto M_{B,1} \times M_{B,2} \times \cdots \times M_{B,S}$ and of the sensor sub path $M_B^{\text{sensor}} \propto M_{B,S+1} \times M_{B,S+2} \times \cdots \times M_{B,S+T}$. After connecting the two sub-paths, the integrand is:

$$P_B(\overline{p}_{L+2}) \propto L_{e,B} \times M_B^{light} \times M_B^{sensor} \tag{10}$$

The light sub-path starts from the light source, then hits the surfaces from 1 to S. It gives the block matrix $E_B \times M_B^{\text{light}}$ of three N-element vectors. The sensor sub-path hits the surfaces $S+T$ to $S+1$. The matrix product being not commutative, $E_B \times M_B^{light}$ and M_B^{sensor} are computed in opposite directions.

Eq (10) is computationally expensive. For N spectral bands, a sensor sub-path throughput is a $3N \times 3N$ matrix. For optimization, diagonal matrices are considered whenever possible when multiplying matrices, and only $R_l + M_{PSIy}^l + M_{PSII}^l$, M_{PSI}^l, M_{PSII}^l and R_l are stored instead of $M_B^l \propto$

$$\begin{pmatrix} R_l + M_{PSIy}^l + M_{PSII}^l & M_{PSI}^l & M_{PSII}^l \\ 0 & R & 0 \\ 0 & 0 & R \end{pmatrix}$$

because the product of matrices of this form has the same form (*cf.* Appendix 1).

As DART-FT (Malenovský et al., 2021), DART-Lux can import SCOPE η factors vertical profiles for sunlit and shaded leaves to account for the influence of local bioclimatology on leaf-level SIF emission. With the assumption that only PSII emission is affected, we have:

$$M_{B,\eta} \propto \begin{pmatrix} R + M_{PSI} + \eta.M_{PSII} & M_{PSI} & \eta.M_{PSII} \\ 0 & R & 0 \\ 0 & 0 & R \end{pmatrix}$$

Increasing the number of Monte Carlo samples/pixel $N_{samples}$ in the simulated images improves accuracy and increases simulation time. The optimal average $N_{samples}$ depends on the scene properties, pixel size, expected precision and simulation time.

PSI and PSII radiance images (Fig. 12) of the 3×3 km^2 Ripperdan zone illustrate the potential of DART-Lux SIF modelling for large landscapes. It needed 42.9 GB of memory and 2 h 44 min in simulation time with an Intel Xeon W-2295 CPU @ 3.00 GHz (18 cores, 36 threads). DART-FT was not run due to huge computational demands: more than 100 TB of memory and 15000 h of simulation time.

4. Assessment of DART-Lux SIF modelling

Malenovský et al. (2021) validated DART-FT SIF modelling against the SCOPE/mSCOPE model for homogeneous canopies. Here, the accuracy and computer efficiency of DART-Lux SIF modelling are assessed for three canopies, using DART-FT SIF as a reference. DART-Lux is also compared to SCOPE for homogeneous scenes. These model cross-comparisons between models M_1 and M_2 for N spectral bands and a given physical quantity q, are done with the Mean Absolute Relative Difference (MARD):

$$MARD_{M_1/M_2} = \frac{1}{\sum_{i=1}^{N} \Delta\lambda_i} \sum_{i=1}^{N} \frac{|q_{M1,i} - q_{M2,i}|}{q_{M2,i}} \Delta\lambda_i \tag{11}$$

4.1. Study cases

Three vegetation canopies (Fig. 3) are studied. 1) Homogeneous turbid scene: 1 m high, LAI = 1, spherical LAD, nadir observation and solar direction ($\theta_s = 30^\circ, \phi_s = 225^\circ$). 2) Maize crop field: 7.5 m × 5 m scene, 600 maize plants, 0°-180° oriented rows and 40 cm spaced, 15 cm within row plant distance, LAI = 1.9, three viewing directions (nadir; $\theta_v = 30^\circ, \phi_v = 0^\circ$; $\theta_v = 60^\circ, \phi_v = 0^\circ$), and three solar directions ($\theta_s = 42.78^\circ, \phi_s = 82.98^\circ$; $\theta_s = 31.46^\circ, \phi_s = 69.88^\circ$; $\theta_s = 21.41^\circ, \phi_s = 48.32^\circ$). 3) Tree plot: 10 m × 10 m scene, 10 randomly distributed trees with branch and trunk reflectance from the DART spectral database ("*populus_tremuloides_bran*"), LAI = 1.9, nadir viewing direction and ($\theta_s = 30^\circ$, $\phi_s = 225^\circ$). Simulations are over [400–850 nm] with 451 bands ($\Delta\lambda$ = 1 nm) for the homogeneous site and maize field, and 45 bands ($\Delta\lambda$ = 10 nm) for the tree plot. Atmosphere (gas model: USSTD76, aerosol model: RURALV23), leaf biochemistry and structure (Table 1), and ground reflectance "*loam_gravelly_brown_dark*" from the DART database. Spatial resolution is 0.1 m for the tree plot and the homogenous site. It is 0.5 m and 0.01 m for the maize field, with 0.01 m selected to mimick the simulation of images of large scenes. It implied using fewer spectral bands in order to maintain reasonable computational needs for DART-FT: 35 excitation bands over [400–750 nm] and one emission band (λ_c = 765 nm, $\Delta\lambda$ = 1 nm).

4.2. Homogeneous turbid canopy

SCOPE is a reference model for simulating the SIF radiance of homogeneous vegetation. Here, DART-FT and DART-Lux SIF simulate the homogeneous turbid scene of SCOPE as a homogeneous quasi turbid medium for two cases depending if SCOPE simulates or not the energy balance (EB):

- No EB: the η factors are set to one in DART-FT and DART-Lux.
- EB: DART-FT and DART-Lux use the SCOPE η factors for the default meteorological parameters.

Fig. 4 shows DART-Lux, DART-FT and SCOPE PSI and PSII nadir radiance. DART-Lux closely matches DART-FT and, to a lesser extent, SCOPE. Without EB, $MARD_{\text{DART-Lux/DART-FT}}$ is 0.70% for PSI and 0.53% for PSII, and $MARD_{\text{DART-Lux/SCOPE}}$ is 5.24% for PSI and 4.93% for PSII. Without neglect of EB, $MARD_{\text{DART-Lux/DART-FT}}$ is 0.08% for PSI and 0.19% for PSII, and $MARD_{\text{DART-Lux/SCOPE}}$ is 5.57% for PSI and 5.15% for PSII.

4.3. Maize field

The canopy nadir reflectance (Fig. 5) and SIF PSI and PSII radiance (Fig. 6, Table 2) simulated by DART-FT, DART-Lux and SCOPE for the three viewing directions and three sun directions show that:

- DART-Lux and DART-FT match: $MARD_{\text{reflectance}} < 1.3\%$ and $MARD_{\text{SIF radiance}} < 1\%$.
- DART-Lux and DART-FT poorly match SCOPE: $MARD_{\text{reflectance}}$ up to 16% and $MARD_{\text{SIF radiance}}$ from 3% to 19%, depending on the solar and viewing angles, with larger MARD for larger viewing angles.

Table 3 shows the computer time and RAM needs of DART-Lux and DART-FT at 0.5 m and 0.01 m resolutions, and also the main input parameters that influence their computational needs. Compared to DART-FT (200 discrete directions, 8 iterations, illumination step = 10^{-3}m), DART-Lux (7^2 scene repetitions, maximum scattering order = 15, Russian Roulette starts at order 12 with cut-off probability = 0.5) decreases the memory by a factor of ≈34 and computer time by ≈1.4 at 0.5 m resolution. It decreases the memory by ≈48 and computer time by ≈50 at 0.01 m resolution. Fig. 7 shows nadir radiance images at 0.01 m resolution: DART-Lux RGB color composite, and also DART-Lux and DART-FT PSI and PSII nadir radiance images.

DART-FT and DART-Lux were also run using the η factors calculated

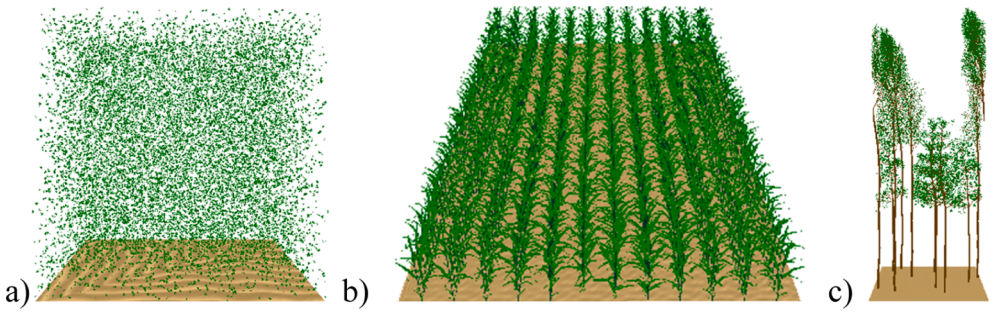

Fig. 3. The simulated 3D mock-ups. a) Homogeneous medium b) Maize field. c) Tree plot.

Table 1
Leaf biochemistry and structure for the three study sites.

Parameter	Symbol	Unit	Homogeneous canopy	Maize field	Tree plot
Leaf structure parameter	N	–	1.8	1.5	1.8
Chlorophyll a + b content	C_{ab}	$\mu g \cdot cm^{-2}$	45	50	30
Carotenoid content	C_{ca}	$\mu g \cdot cm^{-2}$	15	15	10
Water content	C_w	cm	0.009	0.009	0.012
Dry matter content	C_{dm}	$g \cdot cm^{-2}$	0.0020	0.0021	0.0100
FQE for photosystem I	ϕ_{PSI}	–	0.002	0.002	0.002
FQE for photosystem II	ϕ_{PSII}	–	0.01	0.01	0.01

by SCOPE with its default meteorological input parameters. Although these η factors should depend on the canopy 3D architecture, we made this approximation (*i.e.*, application of 1D information in a 3D model) because of the unavailability of 3D energy balance model. DART-Lux and DART-FT match as for the case "No energy balance": the MARD for canopy SIF radiance and for canopy reflectance (not shown here) keep the same order of magnitude. The differences with SCOPE are also similar.

4.4. Trees plot simulation

The reflectance and SIF radiance simulated for a solar direction ($\theta_s = 30^\circ, \phi_s = 225°$) of DART-Lux ($17^2$ scene repetitions, maximum scattering order = 15, Russian Roulette starts at order 12 with cut-off probability = 0.5, 200 samples per pixel) are in agreement with DART-FT (100 discrete directions, 8 iterations, illumination step = 10^{-3} m) (Fig. 8): MARD is 0.27% for reflectance and<0.15% for SIF radiance, with memory need reduced by ~ 13 and computer time by more than 5 times (Table 4). Fig. 9 shows the root mean square deviation (RMSD) of DART-Lux and DART-FT PSI and PSII radiance with the number of samples/pixel (*i.e.*, simulation time).

Fig. 10 shows the pixel-wise comparison of DART-FT and DART-Lux PSII images at 765 nm, for 200 samples/pixel and for 1000 samples/pixel. The pixel-wise MARD is computed by replacing the average on spectral bands by the average on the image pixels. The pixel-wise MARD for 200 samples/pixel (16.89%) is larger than for 1000 samples/pixel (13.88%). Inversely, the R^2 slightly increases from 200 samples/pixel to 1000 samples/pixel. The MARDs are much higher than the spectrally averaged MARD for the total scene (0.15%, Fig. 8) in particular because the images have many pixels. The MARDs and R^2 for PSI (not shown here) are nearly the same as for PSII.

Fig. 11 shows DART-Lux images of the tree plot with 1000 samples/pixel. The SIF signal from the bare ground comes from the SIF radiation emitted by the vegetation that is scattered by the ground.

5. Discussion

DART-FT and DART-Lux have different radiative transfer modelling strategies. DART-FT is deterministic. It tracks radiation fluxes in N discrete directions that sub-divide the 4π space with an iterative approach that scatters at iteration $i+1$ radiation intercepted in iteration i (Gastellu-Etchegorry et al., 1996). DART-Lux is probabilistic. Indeed, it uses Monte-Carlo integration techniques to solve the LTE by sampling the possible light paths, evaluating their contributions, and giving higher importance weights to most likely paths (Wang et al., 2022).

For small scenes, DART-Lux and DART-FT SIF closely match, with relative difference always smaller than 2%. This difference is small enough to be explained by the parameters that drive the precision of DART-Lux (*e.g.*, number of samples/pixel) and DART-FT (*e.g.*, dimension of voxels, numbers of discrete directions, etc.). For these scenes, compared to DART-FT, DART-Lux efficiency is not as pronounced as for

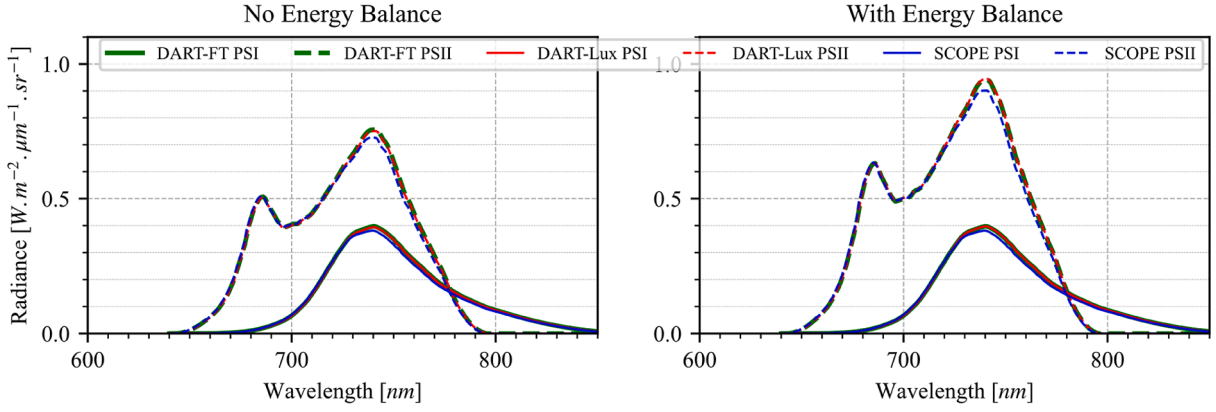

Fig. 4. Homogeneous site: DART-FT, DART-Lux and SCOPE PSI and PSII nadir radiance, without (left) and with (right) computation of the canopy energy balance.

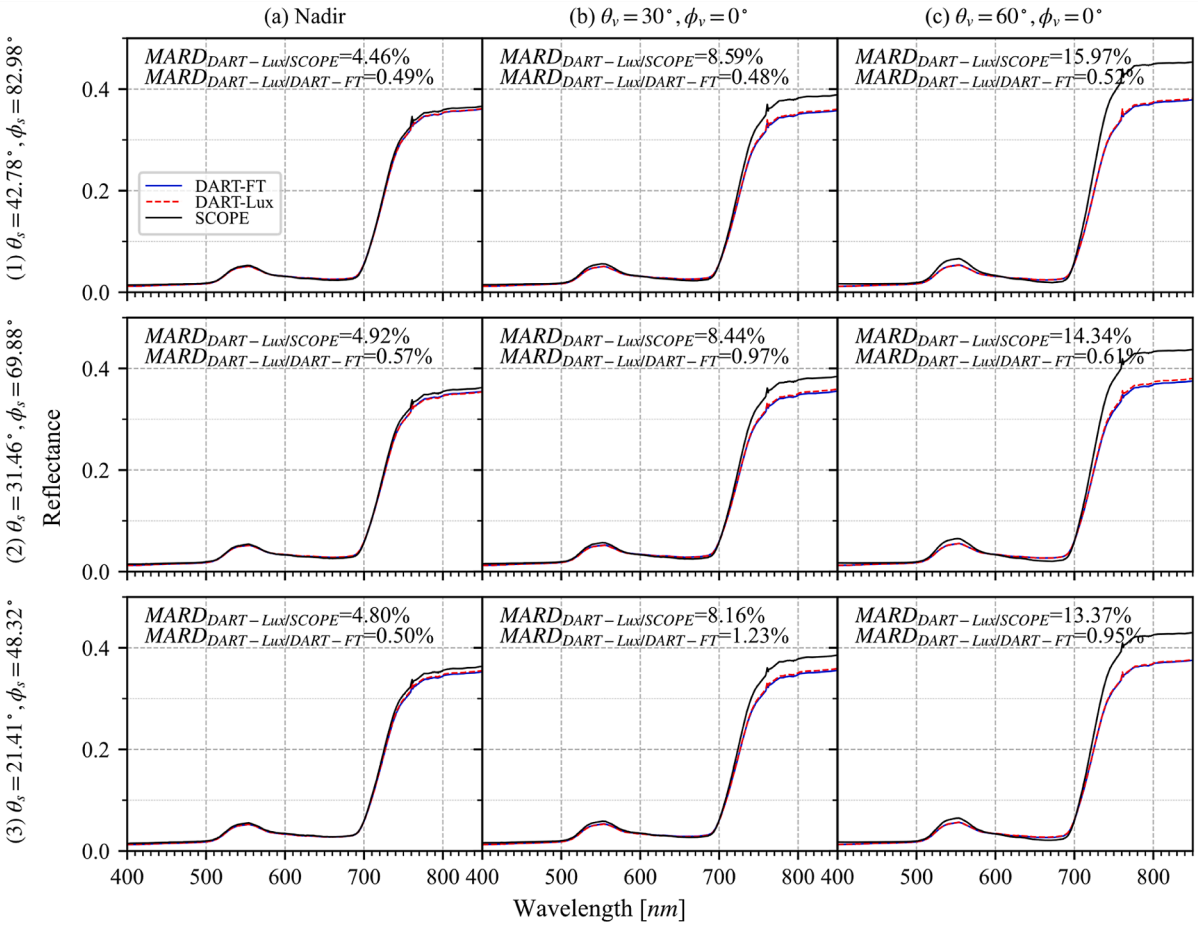

Fig. 5. Maize field: DART-FT, DART-Lux and SCOPE reflectance for 3 solar directions and 3 viewing directions with no account of bioclimatology on SIF emission.

larger sites as Ripperdan (Fig. 12).

5.1. Homogeneous vegetation

DART-Lux closely matches DART-FT and also SCOPE to a lesser extent. Its relative differences are<1% with DART-FT, and ≈5% for SCOPE. Four major factors can explain that differences are higher for SCOPE. 1) SCOPE simulates radiative transfer with four fluxes and assumes the isotropy of downward and upward scattered radiation, which is not exact (except for the special case of exactly horizontal leaves). On the other hand, DART-FT uses many (here: 200) discrete directions, which allows an accurate representation of the anisotropy of the downward and upward scattered radiation. DART-Lux simulates this anisotropy even more accurately than DART-FT because it can track photons in any direction. 2) SCOPE discretizes the LAD with 13 leaf zenith angles, whereas DART-FT and DART-Lux randomly sample the LAD with a number of samples equal to the number of facets used to simulate the quasi-turbid medium. DART and SCOPE more closely match (results not shown here) by introducing into the code of SCOPE a more accurate LAD with 90 leaf zenith angles. 3) The quasi-turbid medium is not exactly the turbid medium of SCOPE because its facets cannot be infinitely small and infinitely numerous. 4) The application of the SCOPE η factors in SCOPE, on the one hand, and in DART-FT and DART-Lux, on the other hand, differs. Indeed, SCOPE applies vertical profiles of η factors to homogeneous layers and DART to facets with interpolations on the η. For this simulation, the η factors (*i.e.*, impact of local climatology) do not impact PSI SIF radiance and increase PSII radiance by ≈25%.

Maize field: the DART-FT and DART-Lux total and SIF radiance closely match and tend to be smaller than for SCOPE, especially for oblique viewing directions, with relative difference possibly larger than 25% for PSII in the NIR. This difference is explained by the canopy 3D architecture (3D maize plants, rows) with the clumping of the maize plants in DART, whereas for SCOPE, the vegetation is homogeneous which is more effective for intercepting radiation and therefore for SIF emission, and also for allowing the emitted SIF radiation to escape the canopy. The $MARD_{DART-SCOPE}$ exceeds 10% in most configurations and increases to reaches 18% for the oblique viewing angle $\theta_v = 60^{\circ}$. Indeed, in SCOPE simulations, radiation interception and therefore SIF emission occur mostly at the top layers of the canopy. When θ_v increases, the SIF seen by the sensor increases because the contribution of the top layers to the signal increases. Similarly, for the 3D maize scene, the SIF seen by the sensor from the plants tends to increase when θ_v increases. However, in these simulations, this increase is less important than for 1D because the viewing direction is parallel to the maize rows and therefore the soil, that does not emit SIF, keeps to be seen by the sensor when θ_v increases. As with the homogeneous canopy, local bioclimatology (*i.e.*, η factors) greatly influences SIF emission, and therefore the canopy SIF radiance. Also, at 0.01 m resolution, DART-Lux deduces by ≈50 the memory usage and simulation time of DART-FT.

5.2. Tree plot

The pixel-wise RMSD (Fig. 10) of the DART-Lux and DART-FT SIF radiance images decreases with the number of samples/pixel in DART-Lux. This is explained by the decrease of the Monte Carlo noise in DART-Lux. For example, the pixel-wise MARD decreases from 16.89% for 200 samples/pixel down to 13.88% with 1000 samples/pixel. Here, convergence occurs for ≈ 1000 samples/pixel. The optimal number of

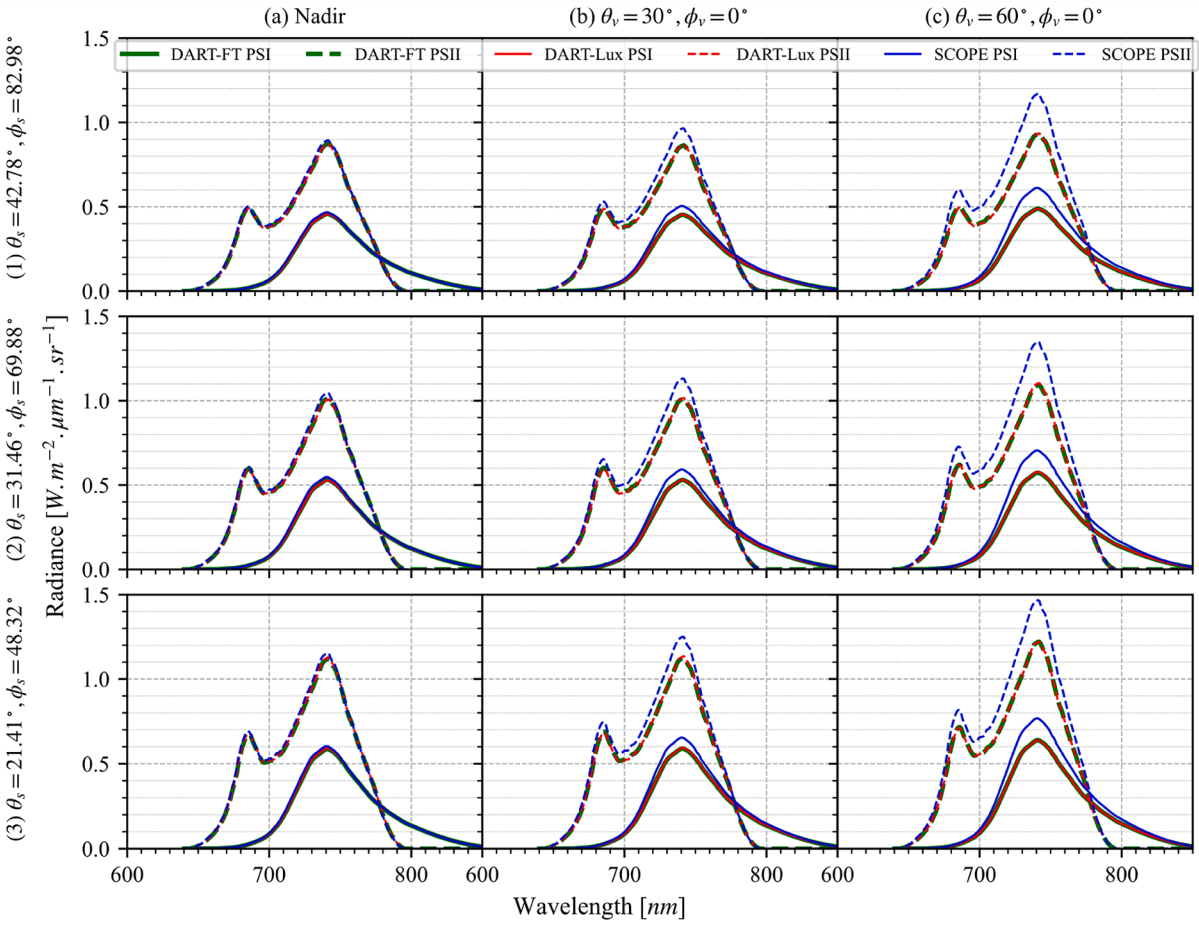

Fig. 6. Maize field: DART-FT, DART-Lux and SCOPE SIF PSII and PSII radiance, for 3 solar directions and 3 viewing directions with no account of bioclimatology on SIF emission.

Table 2
Maize field: MARD of DART-Lux canopy SIF PSI and PSII radiance compared to DART-FT and SCOPE for 3 viewing directions and 3 sun directions.

	Nadir	$\theta_v = 30°$, $\phi_v = 0°$	$\theta_v = 60°$, $\phi_v = 0°$
$\theta_s = 42.78°\ \phi_s = 82.98°$	$MARD_{DART-Lux/DART-FT}$ (PSI, PSII) : (0.46%, 0.44%)	(0.56%, 0.42%)	(0.67%, 0.58%)
	$MARD_{DART-Lux/SCOPE}$ (PSI, PSII) : (3.19%, 4.24%)	(9.61%, 7.81%)	(18.84%, 14.51%)
$\theta_s = 31.46°\ \phi_s = 69.88°$	$MARD_{DART-Lux/DART-FT}$ (PSI, PSII) : (0.53%, 0.43%)	(0.76%, 0.61%)	(0.71%, 0.40%)
	$MARD_{DART-Lux/SCOPE}$ (PSI, PSII) : (4.04%, 4.30%)	(10.04%, 8.03%)	(16.78%, 12.87%)
$\theta_s = 21.41°\ \phi_s = 48.32°$	$MARD_{DART-Lux/DART-FT}$ (PSI, PSII) : (0.88%, 0.63%)	(0.92%, 0.67%)	(0.29%, 0.27%)
	$MARD_{DART-Lux/DART-FT}$ (PSI, PSII) : (3.20%, 4.06%)	(9.05%, 7.77%)	(15.54%, 11.67%)

Table 3
Maize field: input parameters and computational needs of DART-FT and DART-Lux.

		DART-FT	DART-Lux		
5 m spatial resolution, 451 spectral bands	Viewing direction	All upward discrete directions	Nadir	$\theta_v = 30°$, $\phi_v = 0°$	$\theta_v = 60°$, $\phi_v = 0°$
	Computer time	1 h 31 min	1 h 7 min	1 h 9 min	1 h 2 min
	Samples per pixel	–	100	120	180
	Memory (GB)	51	1.5		
0.01 m spatial resolution, 36 spectral bands	Viewing direction	All upward discrete directions	Nadir		
	Computer time	8 h 13 min	10 min 10 s		
	Samples per pixel	–	20		
	Memory (GB)	105.8	8.2		

samples/pixel depends on several factors including the expected accuracy on scene radiance, and the spatial extent and complexity of the studied landscape. The accuracy of the representation of the 3D landscape should also be considered.

Because Monte Carlo-based radiative transfer models are expected to be more accurate than discrete ordinate models, and because the BDPT algorithm is unbiased (Wang et al., 2022), the convergence of $RMSD_{DART-FT-DART-Lux}$ is probably an indication of the accuracy of DART-FT, with DART-Lux giving the exact value.

Results stress that the reduction of simulation time $CT_{FT/Lux} = \frac{\text{DART-FT computer time}}{\text{DART-Lux computer time}}$ of DART-Lux relative to DART-FT can be very important, especially for large and complex scenes. $CT_{FT/Lux} \approx 5800$ for

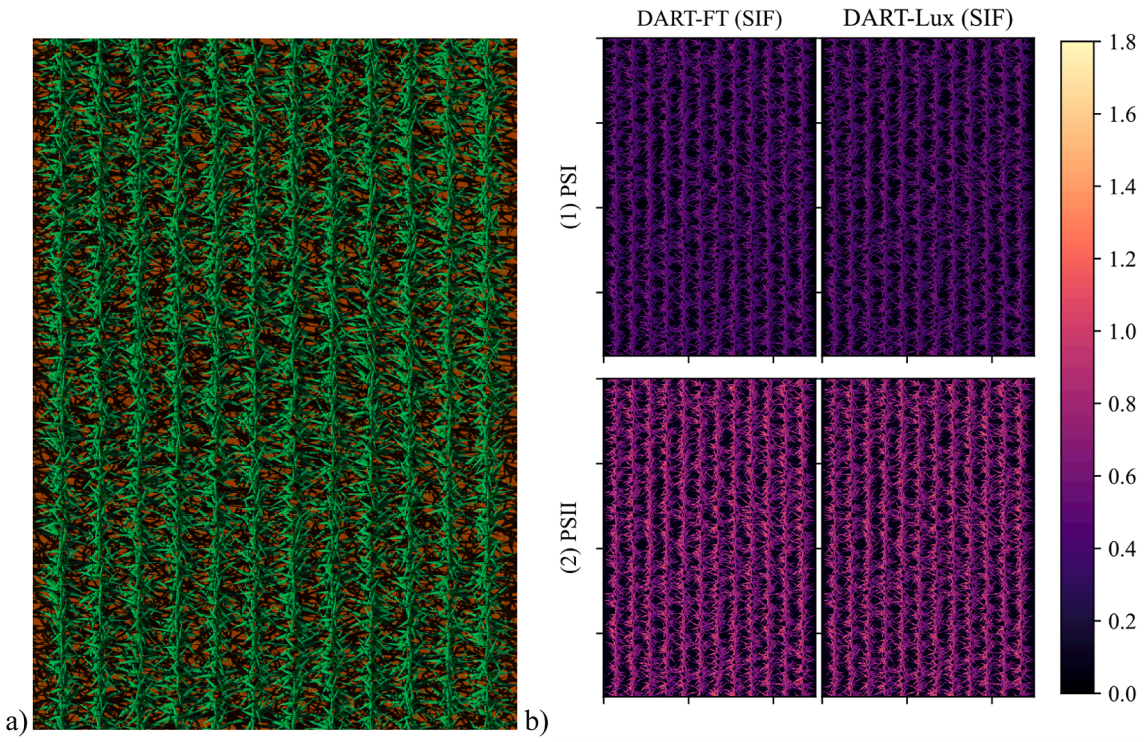

Fig. 7. Maize field: nadir radiance images at 1 cm resolution ($W{\cdot}m^{-2}{\cdot}\mu m^{-1}{\cdot}sr^{-1}$). a) DART-Lux RGB color composite. b) DART-FT and DART-Lux SIF (PSI and PSII). $\lambda_c = 765$ nm, $\Delta\lambda = 1$ nm.

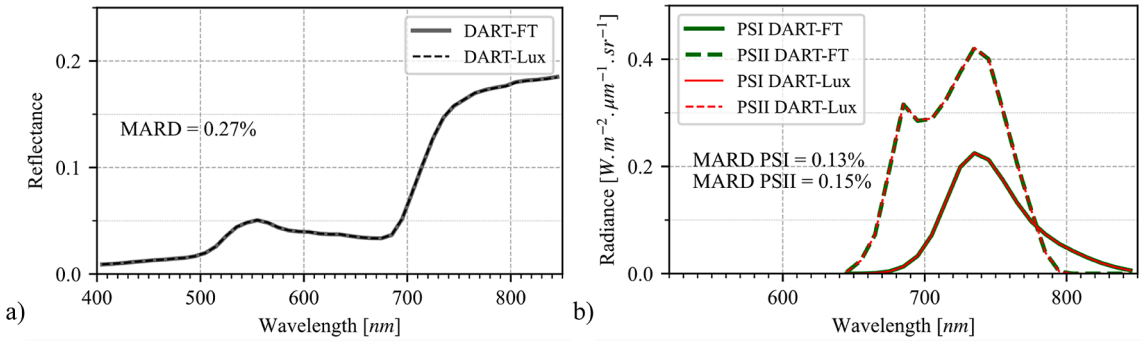

Fig. 8. Tree plot: DART-Lux and DART-FT total (a) and PSI and PSII (b) nadir spectral radiance.

Table 4
Computational needs of DART-FT and DART-Lux for the tree plot simulation (spatial resolution: 0.1 m, 45 spectral bands).

	DART-FT	DART-Lux
Computer time (min)	22	4
Memory (GB)	9.2	0.715

the Ripperdan site. Indeed, the simulation time of DART-FT greatly increases with the number of facets, conversely to DART-Lux if the number of samples/pixel remains constant. Also, $CT_{FT/Lux}$ decreases with the number of simulated spectral bands. Indeed, the DART-FT forward flux tracking simulates SIF with vector-to-matrix products which gives a number of multiplication operations proportional to N^2, with N the number of spectral bands. On the other hand, because DART-Lux path tracing is bi-directional, for rays traced in the backward direction, the SIF emission is modelled by a matrix-to-matrix product which gives a number of multiplication operations proportional to N^3. In the absence of SIF simulation, $CT_{FT/Lux}$ is relatively independent of the number of spectral bands.

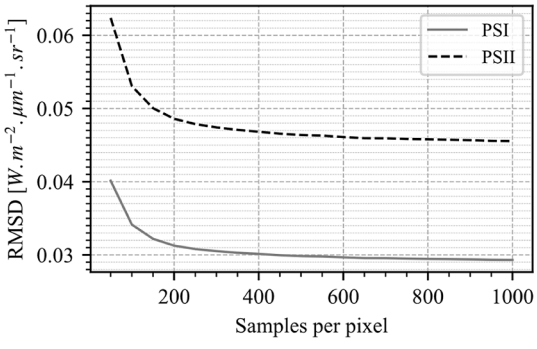

Fig. 9. RMSD of the DART-Lux and DART-FT PSI and PSII radiance images at 765 nm as a function of the number of samples/pixel in DART-Lux.

Because it usually needs much less RAM than DART-FT for complex scenes especially if it uses the cloning approach (Wang et al., 2022),

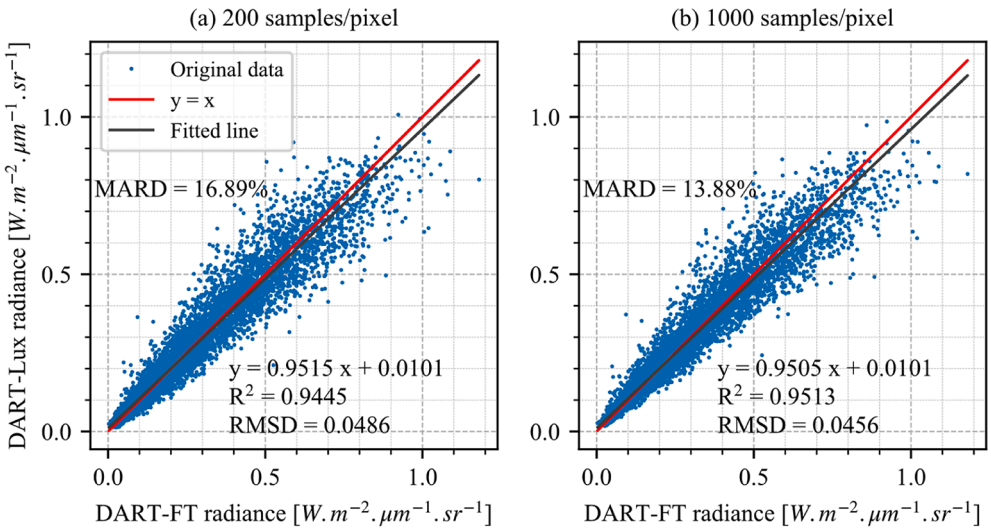

Fig. 10. Pixel-wise comparison of DART-FT and DART-Lux PSII radiance images with samples/pixel = 200 (a) and 1000 (b). $\theta_s = 30^\circ$, $\varphi_s = 225^\circ$ $\lambda_c = 765$ nm, $\Delta\lambda = 10$ nm.

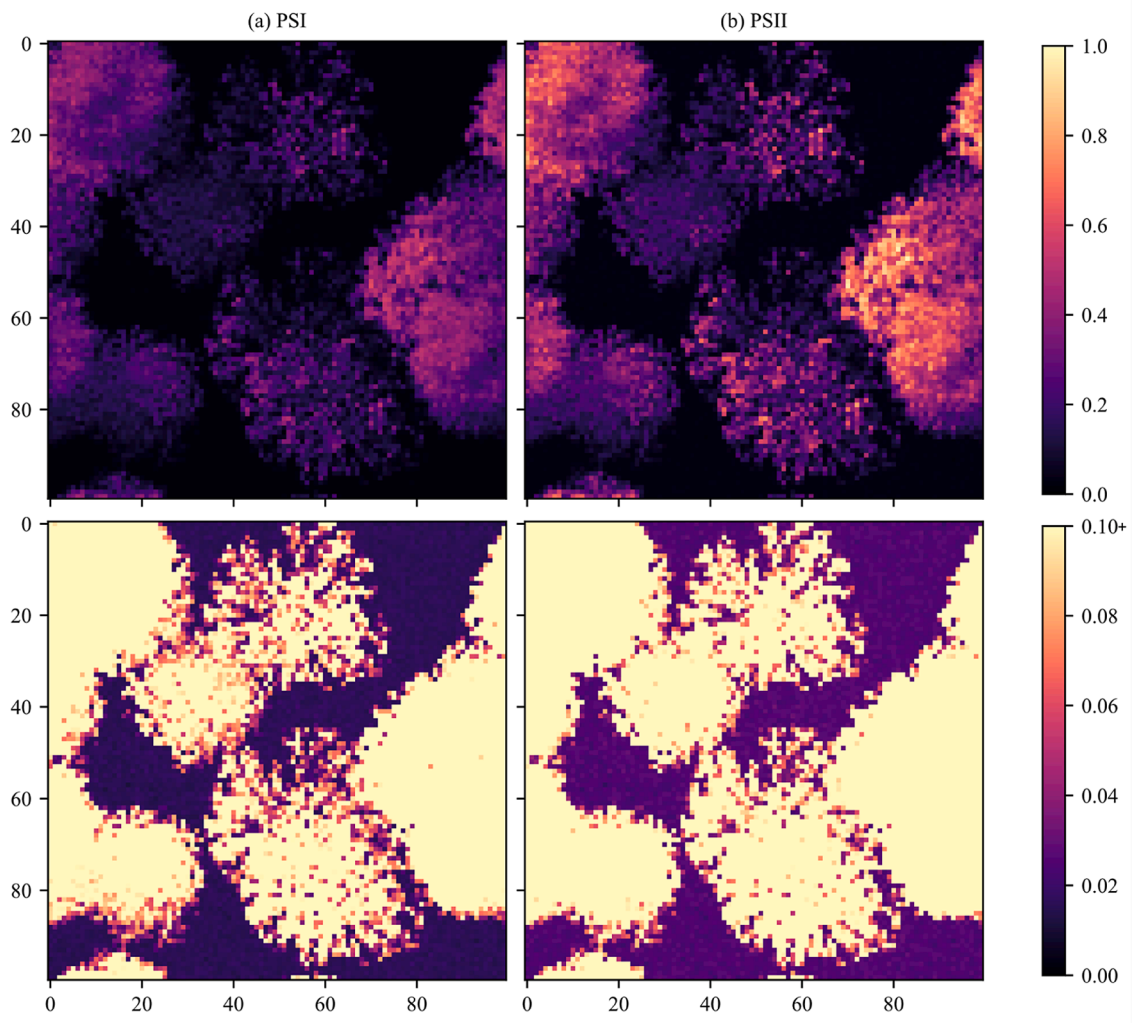

Fig. 11. Tree plot: DART-Lux PSI and PSII SIF nadir radiance images (W.m^{-2}.μm^{-1}.sr^{-1}), with normal (top) and stretched (bottom) color scales. $\lambda_c = 765$ nm, $\Delta\lambda = 10$ nm.

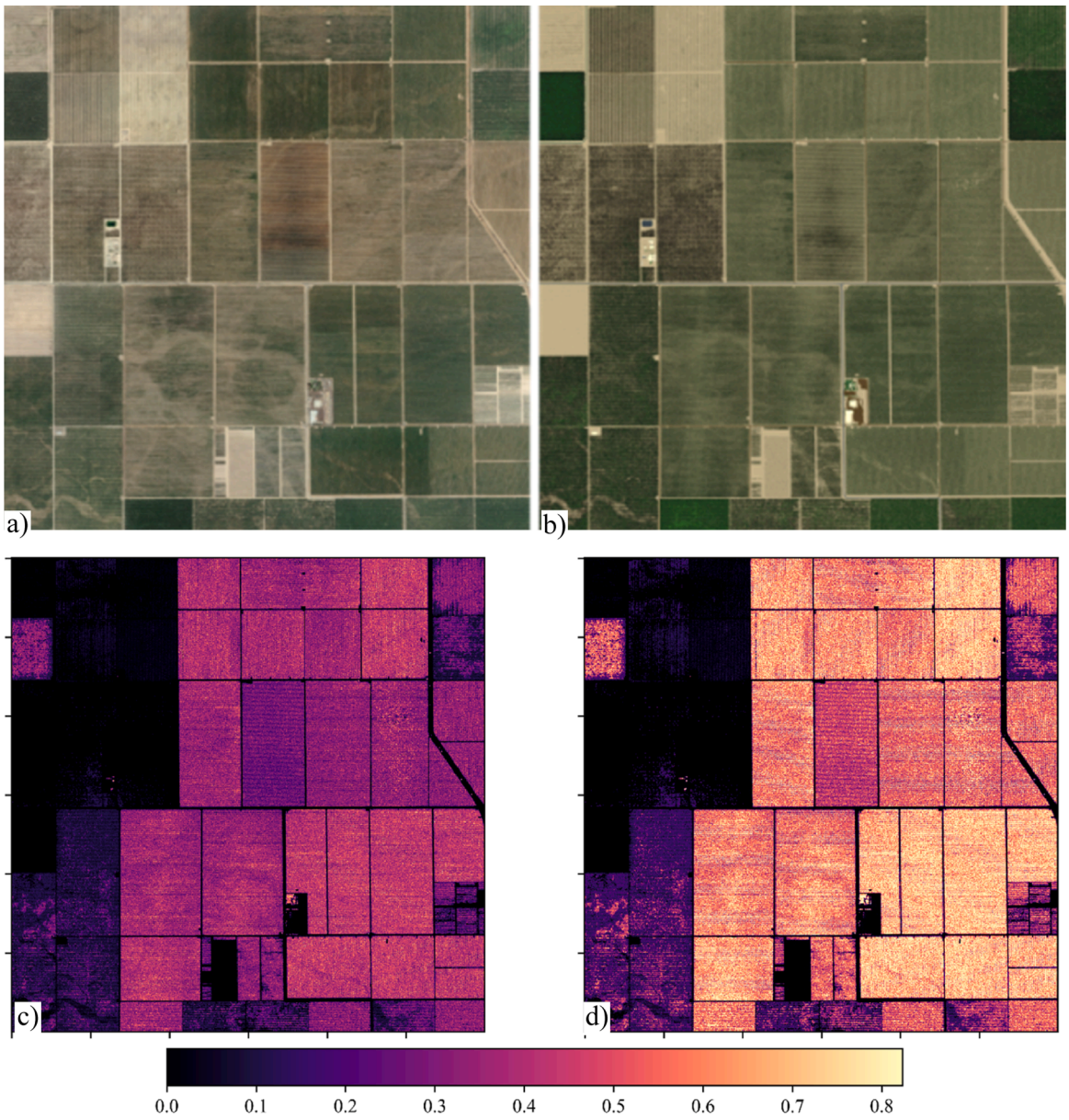

Fig. 12. Ripperdan 3 × 3 km^2 agricultural site (vineyards and trees), USA (36° 55′ N, 119° 58′ W). a) Google image used to create the DART-Lux's 3D scene. b) DART-Lux RGB color composite. DART-Lux PSI (c) and PSII (d) radiance images ($W.m^{-2}.\mu m^{-1}.sr^{-1}$) at 760 nm simulated with 100 bands in [400 nm − 750 nm]). SIF radiance is null for the road (top right), bare earth fields (top left) and built areas (bottom center). DART-Lux images are at 5 m spatial resolution.

DART-Lux is well adapted to large and complex landscapes for which DART-FT can be inoperative due to hardware constraints. Cloning can be used for elements of the simulated landscape are identical except for a geometric transformation: only a single 3D object and a specific geometric transformation (*i.e.*, spatial shift and scaling-rotation matrix) for each clone are stored in memory. Then, the memory needed in DART-Lux increases very little with the number of scene elements, conversely to DART-FT because a geometric transformation matrix usually needs much less memory than a 3D object. Moreover, for DART-Lux, the computation time does not increase a lot when the scene complexity (*i.e.*, total number of scene facets) increases since the algorithmic complexity of Monte Carlo methods depend only on the number of samples, conversely to DART-FT where the total number of tracked rays highly increases with the scene complexity. This makes DART-Lux more computational efficiency for large landscapes, which may be impossible for DART-FT due to hardware limitations. This is illustrated by the 3 × 3km^2 SIF radiance image of Ripperdan (Fig. 12). Indeed, its simulation only needed 42.9 GB of computer memory and 2 h 44 min of computation time for DART-Lux and was impossible for DART-FT.

6. Conclusions

We designed a new SIF radiative transfer modelling that adapts the equations governing the SIF emission to the Bidirectional Path Tracing (BDPT) algorithm, used in DART-Lux, that constructs light paths from the light source and from the sensor. This is a novel SIF modelling approach. Indeed, apart from DART-Lux, to our knowledge, all Monte Carlo RT models that simulate SIF (*e.g.*, FLiES-SIF, FluorFLIGHT, FluorWPS, FluCVRT) use forward tracing, although the BDPT algorithm is more powerful for simulating SIF images. Adapting the BDPT algorithm to SIF modelling greatly improves the efficiency of DART for SIF images simulation, due to the efficiency of backward tracing, especially for sensors with narrow fields of view (Disney et al., 2000).

For that, we adapted the equations that allow to compute the SIF

emission for the BDPT algorithms. The new equations allow to compute the radiance starting both from the light source and from the sensor, and to obtain the total signal (scattered + SIF radiance) in addition to the SIF radiance components per photosystem separately. Simulations conducted with simple 3D canopies illustrated that DART-Lux and DART-FT SIF images have a good agreement. In addition, DART-Lux and 1D SCOPE gave similar total and SIF radiance values when using a very similar scene representation (*i.e.*, homogeneous turbid medium and quasi-turbid medium). They tend to greatly differ if the 3D architecture of the studied landscape is considered. To account for the effect of local climatological conditions (*e.g.*, leaf temperature) on leaf-level SIF emission, DART-Lux can be coupled with the 1D energy balance module of SCOPE by importing vertical profiles of η factors, similarly to DART-FT.

Compared to DART-FT, DART-Lux SIF modelling greatly decreases computational needs (*i.e.*, RAM and computer time). This decrease was by ≈50 times for the maize field with a spatial resolution equal to 0.01 m, and was larger than 10^3 for the 3×3 km^2 Ripperdan agricultural site. This makes DART a powerful model to simulate SIF images of large and complex landscapes, with many spectral bands. It opens new horizons for RS studies of vegetation. The novel SIF simulation in DART-Lux is already in the released DART versions (v1152 onwards) (https://dart.omp.eu).

CRediT authorship contribution statement

Omar Regaieg: Methodology, Software, Validation, Data curation, Visualization, Writing – original draft. **Nicolas Lauret:** Methodology, Software. **Yingjie Wang:** Writing – review & editing. **Jordan Guilleux:** Software. **Eric Chavanon:** Software. **Jean-Philippe Gastellu-Etchegorry:** Conceptualization, Methodology, Writing – review & editing, Supervision, Project administration, Funding acquisition.

Declaration of Competing Interest

The authors declare that they have no known competing financial interests or personal relationships that could have appeared to influence the work reported in this paper.

Data availability

The authors do not have permission to share data.

Acknowledgements

This work was funded as the “Fluo3D” project by the TOSCA program of the French National Space Agency (Centre National d’Etudes Spatiales), and by the CNRS (Centre National de la Recherche Scientifique) through the 80|Prime program.

Appendix 1. . Block matrices product

The product of the block matrices $M_1 = \begin{pmatrix} A_1 & B_1 & C_1 \\ 0 & D_1 & 0 \\ 0 & 0 & D_1 \end{pmatrix}$ and $M_2 = \begin{pmatrix} A_2 & B_2 & C_2 \\ 0 & D_2 & 0 \\ 0 & 0 & D_2 \end{pmatrix}$, with D_1 and D_2 diagonal matrices, is a block matrix with same form as M_1 and M_2:

$$M_1 \times M_2 = \begin{pmatrix} A_1 & B_1 & C_1 \\ 0 & D_1 & 0 \\ 0 & 0 & D_1 \end{pmatrix} \times \begin{pmatrix} A_2 & B_2 & C_2 \\ 0 & D_2 & 0 \\ 0 & 0 & D_2 \end{pmatrix}$$

$$= \begin{pmatrix} A_1 \times A_2 & A_1 \times B_2 + B_1 \times D_2 & A_1 \times C_2 + C_1 \times D_2 \\ 0 & D_1 \times D_2 & 0 \\ 0 & 0 & D_1 \times D_2 \end{pmatrix}$$

where $D_1 \times D_2$ is a diagonal matrix.

References

Braghiere, R.K., Wang, Y., Doughty, R., Sousa, D., Magney, T., Widlowski, J.-L., Longo, M., Bloom, A.A., Worden, J., Gentine, P., Frankenberg, C., 2021. Accounting for canopy structure improves hyperspectral radiative transfer and sun-induced chlorophyll fluorescence representations in a new generation Earth System model. Remote Sens. Environ. 261, 112497 https://doi.org/10.1016/j.rse.2021.112497.

Cormen, T.H., Leiserson, C.E., Rivest, R.L., Stein, C., 2009. Introduction to Algorithms, 3rd ed. MIT Press.

Damm, A., Guanter, L., Paul-Limages, E., van der Tol, C., Hueni, A., Buchmann, N., Eugster, W., Ammann, C., Schaepman, M.E., 2015. Far-red sun-induced chlorophyll fluorescence shows ecosystem - specific relationships to gross primary production: An assessment based on observational and modeling approaches. Remote Sens. Environ. 166, 91–105. https://doi.org/10.1016/j.rse.2015.06.004.

Disney, M.I., Lewis, P., North, P.R.J., 2000. Monte Carlo ray tracing in optical canopy reflectance modelling. Remote Sens. Rev. 18 (2–4), 163–196. https://doi.org/10.1080/02757250009532389.

Gastellu-Etchegorry, J.-P., Demarez, V., Pinel, V., Zagolski, F., 1996. Modeling radiative transfer in heterogeneous 3-D vegetation canopies. Remote Sens. Environ. 58 (2), 131–156. https://doi.org/10.1016/0034-4257(95)00253-7.

Guanter, L., Zhang, Y., Jung, M., Joiner, J., Voigt, M., Berry, J.A., Frankenberg, C., Huete, A.R., Zarco-Tejada, P., Lee, J.-E., Moran, M.S., Ponce-Campos, G., Beer, C., Camps-Valls, G., Buchmann, N., Gianelle, D., Klumpp, K., Cescatti, A., Baker, J.M., Griffis, T.J., 2014. Global and time-resolved monitoring of crop photosynthesis with chlorophyll fluorescence. Proc. Natl. Acad. Sci. 111 (14), E1327–E1333. https://doi.org/10.1073/pnas.1320008111.

Hernández-Clemente, R., North, P.R.J., Hornero, A., Zarco-Tejada, P.J., 2017. Assessing the effects of forest health on sun-induced chlorophyll fluorescence using the FluorFLIGHT 3-D radiative transfer model to account for forest structure. Remote Sens. Environ. 193, 165–179. https://doi.org/10.1016/j.rse.2017.02.012.

Hornero, A., North, P.R.J., Zarco-Tejada, P.J., Rascher, U., Martín, M.P., Migliavacca, M., Hernandez-Clemente, R., 2021. Assessing the contribution of understory sun-induced chlorophyll fluorescence through 3-D radiative transfer modelling and field data. Remote Sens. Environ. 253, 112195 https://doi.org/10.1016/j.rse.2020.112195.

Kallel, A., 2020. FluLCVRT: Reflectance and fluorescence of leaf and canopy modeling based on Monte Carlo vector radiative transfer simulation. J. Quant. Spectrosc. Radiat. Transf. 253, 107183 https://doi.org/10.1016/j.jqsrt.2020.107183.

Kalos, M.H., Whitlock, P.A., 1986. Monte Carlo methods Vol. 1:, Basics..

Liu, W., Atherton, J., Mõttus, M., Gastellu-Etchegorry, J.-P., Malenovský, Z., Raumonen, P., Åkerblom, M., Mäkipää, R., Porcar-Castell, A., 2019a. Simulating solar-induced chlorophyll fluorescence in a boreal forest stand reconstructed from terrestrial laser scanning measurements. Remote Sens. Environ. 232, 111274 https://doi.org/10.1016/j.rse.2019.111274.

Liu, X., Guanter, L., Liu, L., Damm, A., Malenovský, Z., Rascher, U., Peng, D., Du, S., Gastellu-Etchegorry, J.-P., 2019b. Downscaling of solar-induced chlorophyll fluorescence from canopy level to photosystem level using a random forest model. Remote Sens. Environ. 231, 110772 https://doi.org/10.1016/j.rse.2018.05.035.

Liu, W., Luo, S., Lu, X., Atherton, J., Gastellu-Etchegorry, J.-P., 2020. Simulation-Based Evaluation of the Estimation Methods of Far-Red Solar-Induced Chlorophyll Fluorescence Escape Probability in Discontinuous Forest Canopies. Remote Sens. (Basel) 12 (23), Article 23. https://doi.org/10.3390/rs12233962.

Malenovský, Z., Regaieg, O., Yin, T., Lauret, N., Guilleux, J., Chavanon, E., Duran, N., Janoutová, R., Delavois, A., Meynier, J., Medjdoub, G., Yang, P., van der Tol, C., Morton, D., Cook, B.D., Gastellu-Etchegorry, J.-P., 2021. Discrete anisotropic radiative transfer modelling of solar-induced chlorophyll fluorescence: Structural impacts in geometrically explicit vegetation canopies. Remote Sens. Environ. 263, 112564 https://doi.org/10.1016/j.rse.2021.112564.

Miller, J., 2005. Development of a Vegetation Fluorescence Canopy Model.

Mohammed, G.H., Colombo, R., Middleton, E.M., Rascher, U., van der Tol, C., Nedbal, L., Goulas, Y., Pérez-Priego, O., Damm, A., Meroni, M., Joiner, J., Cogliati, S., Verhoef, W., Malenovský, Z., Gastellu-Etchegorry, J.-P., Miller, J.R., Guanter, L., Moreno, J., Moya, I., Zarco-Tejada, P.J., 2019. Remote sensing of solar-induced chlorophyll fluorescence (SIF) in vegetation: 50 years of progress. Remote Sens. Environ. 231, 111177 https://doi.org/10.1016/j.rse.2019.04.030.

Nicodemus, F.E. (Fred E. (1978). Self-study manual on optical radiation measurements: Part I–Concepts, Chapters 4 and 5. National Bureau of Standards (U.S.). http://archive.org/details/selfstudymanualo9102nico.

Pharr, M., Jakob, W., Humphreys, G., 2016. Physically Based Rendering: From Theory to Implementation, (3rd ed.). Morgan Kaufmann Publishers Inc.

Porcar-Castell, A., Tyystjärvi, E., Atherton, J., van der Tol, C., Flexas, J., Pfündel, E.E., Moreno, J., Frankenberg, C., Berry, J.A., 2014. Linking chlorophyll a fluorescence to photosynthesis for remote sensing applications: Mechanisms and challenges. J. Exp. Bot. 65 (15), 4065–4095. https://doi.org/10.1093/jxb/eru191.

Regaieg, O., Yin, T., Malenovský, Z., Cook, B.D., Morton, D.C., Gastellu-Etchegorry, J.-P., 2021. Assessing impacts of canopy 3D structure on chlorophyll fluorescence radiance and radiative budget of deciduous forest stands using DART. Remote Sens. Environ. 265, 112673 https://doi.org/10.1016/j.rse.2021.112673.

Rosema, A., Verhoef, W., Schroote, J., Snel, J.F.H., 1991. Simulating fluorescence light-canopy interaction in support of laser-induced fluorescence measurements. Remote Sens. Environ. 37 (2), 117–130. https://doi.org/10.1016/0034-4257(91)90023-Y.

Sakai, Y., Kobayashi, H., Kato, T., 2020. FLiES-SIF version 1.0: Three-dimensional radiative transfer model for estimating solar induced fluorescence. Geosci. Model Dev. 13 (9), 4041–4066. https://doi.org/10.5194/gmd-13-4041-2020.

Song, L., Guanter, L., Guan, K., You, L., Huete, A., Ju, W., Zhang, Y., 2018. Satellite sun-induced chlorophyll fluorescence detects early response of winter wheat to heat stress in the Indian Indo-Gangetic Plains. Glob. Chang. Biol. 24 (9), 4023–4037. https://doi.org/10.1111/gcb.14302.

van der Tol, C., Verhoef, W., Timmermans, J., Verhoef, A., Su, Z., 2009. An integrated model of soil-canopy spectral radiances, photosynthesis, fluorescence, temperature and energy balance. Biogeosciences 6 (12), 3109–3129. https://doi.org/10.5194/bg-6-3109-2009.

Veach, E., 1998. *Robust monte carlo methods for light transport simulation* [Phd]. Stanford University.

Veach, E., & Guibas, L. J. (1995). Optimally combining sampling techniques for Monte Carlo rendering. Proceedings of the 22nd Annual Conference on Computer Graphics and Interactive Techniques, 419–428. 10.1145/218380.218498.

Verhoef, W., 1984. Light scattering by leaf layers with application to canopy reflectance modeling: The SAIL model. Remote Sens. Environ. 16 (2), 125–141. https://doi.org/10.1016/0034-4257(84)90057-9.

Verrelst, J., Malenovsky, Z., van der Tol, C., Camps-Valls, G., Gastellu-Etchegorry, J.-P., Lewis, P., North, P., Moreno, J., 2019. Quantifying Vegetation Biophysical Variables from Imaging Spectroscopy Data: A Review on Retrieval Methods. Surv. Geophys. 40 (3), 589–629. https://doi.org/10.1007/s10712-018-9478-y.

Vilfan, N., Van der Tol, C., Yang, P., Wyber, R., Malenovský, Z., Robinson, S.A., Verhoef, W., 2018. Extending Fluspect to simulate xanthophyll driven leaf reflectance dynamics. Remote Sens. Environ. 211, 345–356. https://doi.org/10.1016/j.rse.2018.04.012.

Wang, Y., Lauret, N., Gastellu-Etchegorry, J.-P., 2020. DART radiative transfer modelling for sloping landscapes. Remote Sens. Environ. 247, 111902 https://doi.org/10.1016/j.rse.2020.111902.

Wang, Y., Kallel, A., Yang, X., Regaieg, O., Lauret, N., Guilleux, J., Chavanon, E., Gastellu-Etchegorry, J.-P., 2022. DART-Lux: An unbiased and rapid Monte Carlo radiative transfer method for simulating remote sensing images. Remote Sens. Environ. 274, 112973 https://doi.org/10.1016/j.rse.2022.112973.

Yang, P., Verhoef, W., van der Tol, C., 2017. The mSCOPE model: A simple adaptation to the SCOPE model to describe reflectance, fluorescence and photosynthesis of vertically heterogeneous canopies. Remote Sens. Environ. 201, 1–11. https://doi.org/10.1016/j.rse.2017.08.029.

Zhang, Z., Zhang, Y., Porcar-Castell, A., Joiner, J., Guanter, L., Yang, X., Migliavacca, M., Ju, W., Sun, Z., Chen, S., Martini, D., Zhang, Q., Li, Z., Cleverly, J., Wang, H., Goulas, Y., 2020. Reduction of structural impacts and distinction of photosynthetic pathways in a global estimation of GPP from space-borne solar-induced chlorophyll fluorescence. Remote Sens. Environ. 240, 111722 https://doi.org/10.1016/j.rse.2020.111722.

Zhao, F., Dai, X., Verhoef, W., Guo, Y., van der Tol, C., Li, Y., Huang, Y., 2016. FluorWPS: A Monte Carlo ray-tracing model to compute sun-induced chlorophyll fluorescence of three-dimensional canopy. Remote Sens. Environ. 187, 385–399. https://doi.org/10.1016/j.rse.2016.10.036.